Article

Effect of Additive and Current Density on Microstructures and Corrosion Behavior of a Multi-Component NiFeCoCu Alloy Prepared by Electrodeposition

Ying Wang [1], Bingyang Ma [1], Wei Li [2], Peter K. Liaw [3], Songpu Yang [4] and Ning Zhong [4,*]

[1] School of Materials Science, Shanghai Dianji University, Shanghai 201306, China; ywang@sdju.edu.cn (Y.W.)
[2] School of Materials Science and Engineering, University of Shanghai for Science and Technology, Shanghai 200093, China; liwei176@usst.edu.cn
[3] Department of Materials Science and Engineering, The University of Tennessee, Knoxville, TN 37996-2200, USA; pliaw@utk.edu
[4] College of Ocean Science and Engineering, Shanghai Maritime University, Shanghai 201306, China
[*] Correspondence: ningzhong@shmtu.edu.cn; Tel.: +86-21-3828-4827

Abstract: High-entropy alloys (HEAs) have been attracting growing interest for decades due to their unique properties. Electrodeposition provides a low-cost and convenient route for producing classified types of HEAs, compared to other synthesis techniques, making it an attention-grabbing method. However, fabricating high-quality HEAs through electrodeposition in aqueous electrolytes remains a great challenge. In this study, the effects of additives and current densities on the compositions, surface morphologies, microstructures, and corrosion behavior of the electrodeposited NiFeCoCu alloy are studied. The results indicate that saccharin plays a key role in achieving a flat and bright surface for NiFeCoCu coatings, while also relieving the internal stress and improving anti-corrosion properties. Electrodeposition under a current density of 20–40 mA/cm^2 results in a uniform and dense deposit with favorable properties. The present work provides a low-cost and feasible industrial solution for the preparation of HEA coatings, which holds great potential for innovation in the field of HEA coatings through electrodeposition.

Keywords: electrodeposition; high-entropy alloys; coatings; corrosion; microstructure

1. Introduction

High-entropy alloys (HEAs) were first proposed by Cantor et al. [1] and Yeh et al. [2], which have been characterized by a large configuration entropy (usually $\Delta S > 1.5$ R). HEAs usually consist of four or more elements, which have profoundly higher mixing entropies than conventional alloys [3]. HEAs have attracted worldwide attention from scientific researchers to technological engineers since they possess excellent mechanical properties, such as high hardness, strength, and ductility [4–8], good wear resistance [9], and excellent corrosion resistance [10–15]. HEAs also have promising functional applications, such as electrical devices [16] and electrocatalysis [17,18], and energy transformation and storage [19,20].

MCA coatings with the enhanced corrosion resistance have received significant attention from surface-engineering workers due to the combination of good mechanical properties and corrosion protection [21,22]. Several studies indicate that MCA coatings can provide satisfactory protection for ships and ocean engineering, especially in harsh marine environments [23]. There are different methodologies that have been developed for the successful synthesis of MCA coatings, such as laser remelting [24,25], magnetron sputtering [26], laser cladding [27], thermal spraying [28,29], electrochemical reduction of oxides in molten salts [30], mechanical alloying [4], hydrogen reduction of oxide powers [31], and electrochemical deposition [32–34]. All these techniques, except for electrodeposition, are

labeled as having a high equipment cost, having relatively high operating temperatures and energy consumption, and presenting difficulty in controlling the coating morphology and composition. On the other hand, electrodeposition offers a relatively lower equipment intensity and can provide great convenience for obtaining different MCA coating microstructures by selecting different deposition parameters, including the current density, applied voltage, temperature, pH, and deposition time [35]. Therefore, many studies have been carried out to investigate the relationship between the microstructure-properties of different multi-component element-containing solutions with the purpose of optimizing the operation parameters [36,37]. Some studies have focused on the synthesis of MCA coatings from ionic liquids or organic solutions [10,37,38]. Although ionic liquids have the advantage of little hydrogen-gas formation during electrodeposition, their higher cost, compared to aqueous solutions, limits their applications [39].

Therefore, a large amount of work has been conducted to deposit MCA coatings in aqueous baths. Pavithra et al. [40] deposited the FeCoNiCuZn MCA coatings with graphene oxides (GO) as reinforcements and found tunable magnetic properties with the content of GO. Aliyu et al. [41] synthesized and compared the structures and corrosion properties of MnFeCoNiCu MCA coatings with and without GO, and their results suggested that the incorporation of GO could effectively increase the anti-corrosion properties. Haché et al. proposed a theoretical strategy for the fabrication of electrodeposited HEAs with sufficient quality and applied it to NiFeCoW and NiFeCoMo alloys [42]. However, electrodeposition of multi-elements in an aqueous bath is still challenging because of the tremendous difference between metal-ion reduction potentials [34], and the challenge in the fabrication of five or more element alloys with high quality from an aqueous electrolyte. Furthermore, the complexity of the electrolyte solution and the different combinations of deposition parameters also make it a difficult task to successfully deposit the MCA coatings, and the thickness of the MCA coatings is usually around a few microns [43,44]. In addition, there are a limited number of studies on electrodeposited MCAs, compared to traditional fabrication methods [45,46], and it is widely believed that the current intensity would greatly affect the microstructures and properties of electro-deposited coatings. In the present study, because of its anticorrosion and magnetic properties, a NiFeCoCu MCA was selected as a model system for its potential applications in functional materials and devices [47,48]. We investigated the effect of additives and current densities on the morphologies, compositions, and microstructures of deposited MCAs, and the corrosion resistance of MCA coatings was also studied in detail. In addition, saccharin, as one of the commonly used green additives, has been employed as an effective stress reliever and grain refiner in the traditional electrodeposition, such as nickel and chrome plating for attaining a dense and crack-free deposits [49,50]. However, to date, there is no research in the literature concerning the effect of saccharin addition on electrodepositing MCA coatings. Therefore, the effect of saccharin content was also investigated in this work.

In the study, NiCoFeCu MCA coatings were directly deposited from sulfide solutions with or without the saccharin addition by the direct current deposition, and the microstructural evolution, surface morphologies, and corrosion resistance of the NiCoFeCu MCA coatings were studied systematically with varied concentrations of the saccharin and applied current density. The effect of the current density and saccharin addition on the microstructures and properties of MCA coatings was investigated, and the results provide a highly cost-effective and realizable industrial solution for preparing MCA protective coatings [51].

2. Materials and Methods

2.1. Materials

A sulfate electrolyte with varying amounts of saccharin additions was used, which contained boric acid as a buffering agent and sodium citrate as a complexing agent. All chemicals were of an analytical grade and purchased from the Sinopharm Chemical Reagent Co., Ltd. (Shanghai, China). The detailed information about the electrolyte can be found in

Table 1. The aqueous electrolyte for electrodeposition was prepared, using the deionized water, and the pH was adjusted to 4.5 by adding a dilute sulfuric acid. The detailed solution-preparation procedure is as follows: Begin by dissolving sodium citrate in deionized water at a temperature of 50 °C, and then introduce nickel sulfate, followed by cobalt sulfate and copper sulfate, in precise succession. Stir this solution for a duration of 5 h, after which it was gently cooled down to ambient room temperature. Given the susceptibility of iron sulfate to oxidation, it is prudent to employ a separate receptacle. Introduce ascorbic acid and iron sulfate, meticulously stirring until a uniform dissolution is achieved. Subsequently, merge this solution of ferric sulfate with the one from the initial beaker. Maintain the process under the influence of magnetic stirring for another 5 h. During the electro-deposition, the current densities were varied from 20 to 60 mA/cm^2 to study their effect on the microstructures and properties of the HEA coatings. Pure copper sheets (20.0 mm $\times$ 10.0 mm $\times$ 1.0 mm) were used as substrate materials. The substrates were mechanically polished with SiC abrasive papers up to 1200# grade, washed, and cleaned with acetone, and then activated in a 12 weight percent (wt.%) hydrochloric acid solution to obtain a suitable surface condition for electrodeposition. A graphite electrode, 40 mm $\times$ 40 mm, was used as an auxiliary anode. All samples were deposited for 60 min, followed by ultrasonic cleaning in distilled water and kept in a drying oven. To facilitate readability and simplicity, e.g., "FeCoCuNi-saccharin 1 g/L–20 mA/cm^2" (the FCCN deposit was processed with 1 g/L saccharin electrolyte under a current density of 20 mA/cm^2) is abbreviated as "1g T-20mA".

Table 1. Compositions of the electrolytes and electrodeposition conditions.

Bath Ingredients	FCCN-0g T	FCCN-xg T (x = 0.5, 1, 2, 4 g/L Saccharin)
Ferrous sulfate·7H$_2$O (g/L)	8.34	8.34
Nickel sulphate·6H$_2$O (g/L)	131.43	131.43
Cobalt sulfate·6H$_2$O (g/L)	14.05	14.05
Cupric sulfate·5H$_2$O (g/L)	4.00	4.00
Boric acid (g/L)	29.66	29.66
Trisodium Citrate (g/L)	44.00	44.00
Plating temperature (°C)	35	35
Bath volume (mL)	300	300
Bath pH	4.5	4.5
Plating time (minutes)	60	60
Under continuous agitation (rpm)	250	250
Saccharin addition (g/L)	None	0.5, 1, 2, 4, respectively
Current density (mA/cm^2)	20, 40	10, 20, 30, 40, 60

2.2. The Electrochemical Measurements

A CHI 660E workstation was used to perform the electrochemical measurements at room temperature. The cyclic voltammetry (CV) measurements for the deposition process of the HEA were conducted using a three-electrode setup. The glassy carbon served as the working electrode, while a platinum plate (10 mm $\times$ 10 mm) and a saturated calomel electrode were used as the auxiliary and reference electrodes, respectively. All potentials mentioned in the study were referenced to the saturated calomel electrode. The CV experiments were performed in a range of 400 mV to -1100 mV with a scan rate of 30 mV/s, using a 50 mL solution at room temperature. The corrosion behavior analysis of the HEA coatings was performed in a three-electrode cell, using the saturated calomel electrode and platinum foil as the reference and counter electrodes, respectively. The potentiodynamic polarization and electrochemical impedance spectroscopy (EIS) measurements were conducted in a 3.5 wt.% sodium chloride solution at 25 °C. Prior to the tests, the samples were immersed in the chloride solution for 30 min until they reached a stable open circuit potential (E$_{ocp}$). The polarization curves were measured from -0.6 V to 0.1 V with a scanning speed of 1 mV/s, while the EIS data were recorded using a frequency range of 0.01 Hz to 100 kHz with an amplitude of 15 mV. The potentials mentioned in the potentiodynamic polarization

and EIS tests were referenced to saturated calomel electrode. The corrosion-current density for the HEA coatings can be determined, employing the Tafel extrapolation formula [52]. Each electrodeposition experiment was repeated three times to ensure result repeatability for cyclic voltammetry, as well as polarization curves and impedance tests.

2.3. Microstructural Characterization

The surface morphologies of the HEA coatings were observed by a JOEL-7500F scanning electron microscope (SEM) operating at an accelerating voltage of 5 kV. The compositions of the HEA coatings were determined by an Oxford Energy Dispersive X-ray Spectrometer (EDS) attached to the JOEL-7500F.

The phase structures of the HEA coatings were detected and analyzed using an X-ray diffraction technique (XRD) on a RIGAKU SmartLab with Cu K$_\alpha$ radiation. The operating voltage was 30 kV, and the beam current was 30 mA. The diffraction patterns of specimens were recorded from 30° to 100°, and the Scherrer equation was used to estimate the crystallite sizes of different HEA coatings [53].

$$D = k\lambda/\beta\cos\theta \qquad (1)$$

where D denotes the average grain size of the coatings, k represents the Scherrer constant (0.94), λ is the X-ray wavelength of the Cu-K$_\alpha$ line (0.154056 nm), and β is the peak width at a half maximum of the diffraction angle, 2θ.

The relative texture coefficients (RTC) for different HEA coatings were estimated by the following formula [38]:

$$RTC(hkl) = \frac{I(hkl)/I_0(hkl)}{\sum I(hkl)/I_0(hkl)} \qquad (2)$$

where I_0 (h k l) is the intensity of an untextured nickel powder (JCPDF No. 04-0850), and I (h k l) is the intensity of the (h k l) plane of HEA coatings.

3. Results

3.1. The Cyclic Voltammograms of HEA Coatings

Figure 1 shows the cyclic voltammograms acquired, using an electrolyte previously described, with a sweep potential rate of 20 mV/s. The cyclic voltammetry exhibits a similar profile, characterized by the presence of a cathodic peak associated with metal-ion deposition and an anodic peak related to the dissolution of HEA coatings, respectively. Figure 1b is an enlarged part of Figure 1a, where it can be observed that with an increase in the saccharin content, the reduction current peak in the cyclic voltammogram becomes more pronounced. The sample with a saccharin content of 1 g/L exhibits the highest reduction current. As a result, the specific loading of 1 g/L saccharin has been thoroughly investigated, and the obtained results will be presented subsequently.
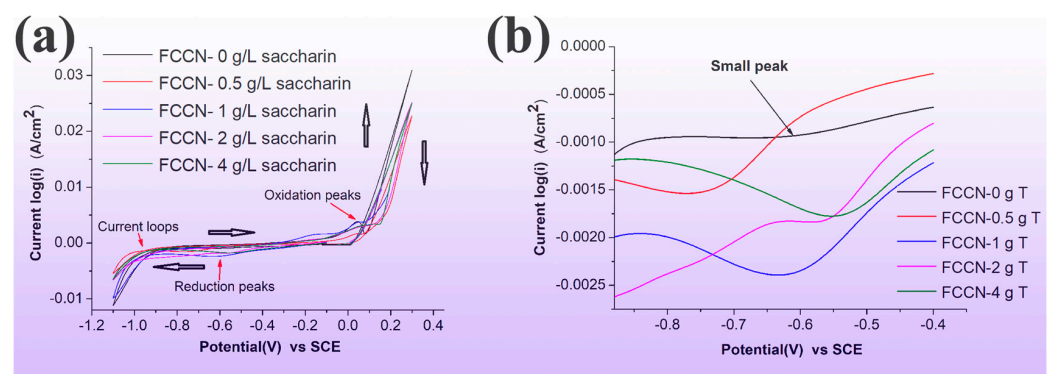

Figure 1. Typical cyclic voltammograms derived from the HEA aqueous solution containing different saccharin loadings at a scan speed of 20 mV/s (**a**) and the enlarged curves between −0.4 V and −0.9 V (**b**).

3.2. The Morphologies and Microstructures of HEA Coatings

The SEM images of the surface morphologies of HEA coatings are depicted in Figure 2. It is evident that the surface morphologies are heavily influenced by the content of saccharin. The HEA coating deposited without the addition of saccharin shows a markedly rough and uneven surface, characterized by the distribution of many colonies assembled by numerous near-spherical particles, as presented in a magnified image shown in Figure 2b. The samples with saccharin all exhibit a smooth surface, with a noticeable reduction in roughness. Additionally, no obvious defects, such as cracks, pinholes, or pores, were observed. From the SEM observation, it can be seen that when the addition of saccharin exceeds 1 g/L, there is not much change in the surface morphologies, which are mainly composed of granular grains, with nodules spanning from tens to hundreds of micrometers in size.
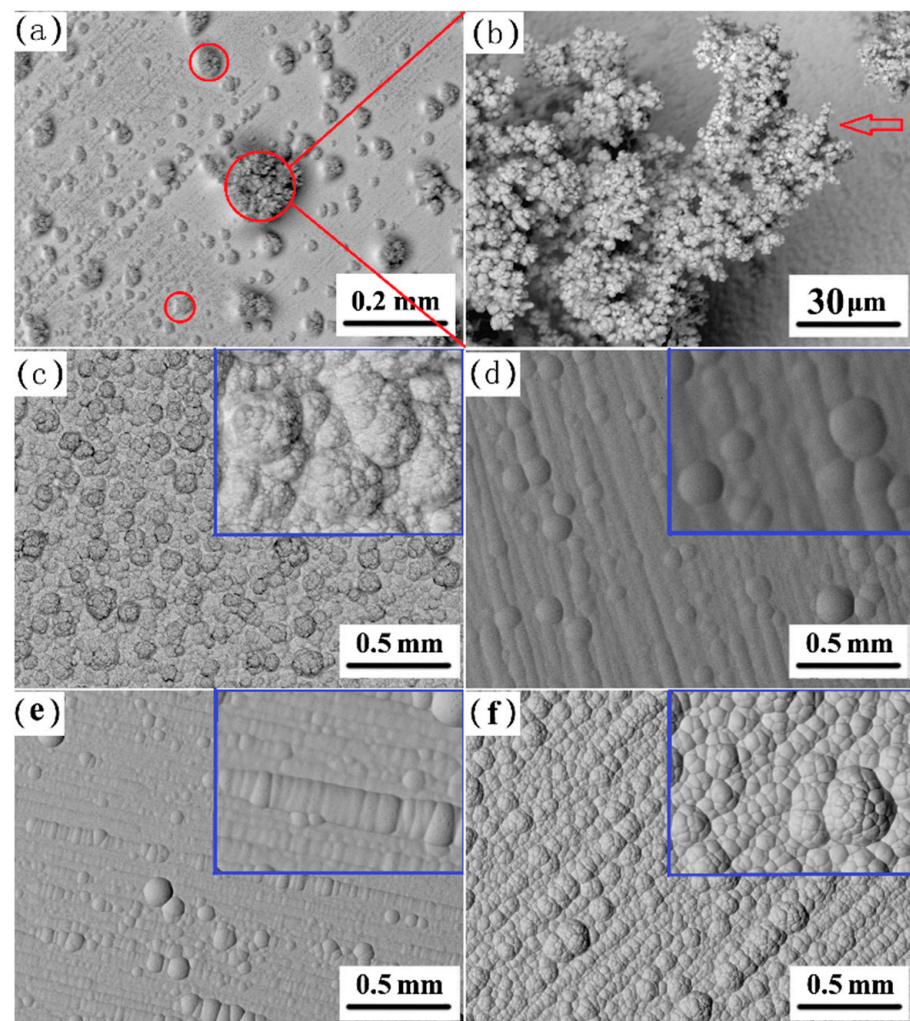

Figure 2. Surface morphologies of (**a**,**b**) FCCN-0g T, (**c**) FCCN-0.5g T, (**d**) FCCN-1g T, (**e**) FCCN-2g T, and (**f**) FCCN-4g T coatings electrodeposited with 20 mA/cm^2 for 60 min, and a photograph with a magnification of X2000 is inserted in the upper right corner of each image.

The EDS spectra of FCCN-0g T-20mA, as shown in Figure 3, clearly indicates that the cauliflower-shaped colonies predominantly consist of the Cu element, while the matrix exhibits a much lower Cu content along with an abundance of other alloying elements. Furthermore, visible cracks can be observed in the FCCN-0g T-20mA coating, which can be attributed to the accumulation of the internal stress [54] and have detrimental effects on the mechanical and anti-corrosion properties of the HEA coating.
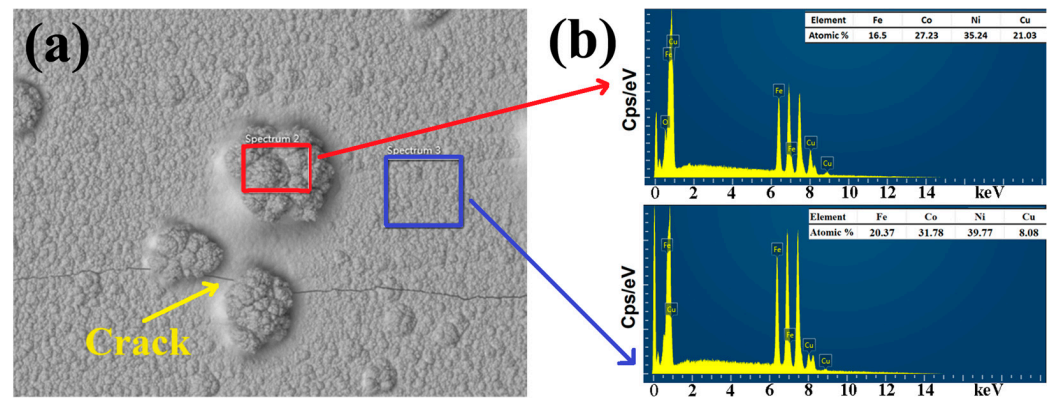
Figure 3. Scanning electron micrographs of FCCN-0g T-20mA deposited with 20 mA/cm^2 for 60 min (**a**) and the corresponding elemental dispersive spectra for the matrix and cauliflower-like structure, respectively (**b**).

3.3. The Phase Constitutes of HEA Coatings

To investigate the impact of the current density on the compositions and microstructures of HEA coatings, the FCCN-1g T electrolyte (with 1 g/L saccharin) was selected, and electrodeposition was conducted at various current densities for 60 min. The XRD patterns of the HEA coatings deposited from the sulfate bath without the saccharin additive are also depicted in Figure 4. All the patterns of the HEA coatings exhibit a typical FCC structure, displaying characteristic peaks corresponding to the (1 1 1), (2 0 0), (2 2 0), (3 1 1), and (2 2 2) planes, with the diffraction angles of approximately 44.5°, 51.8°, 76.4°, 93.0°, and 98.4°, respectively.
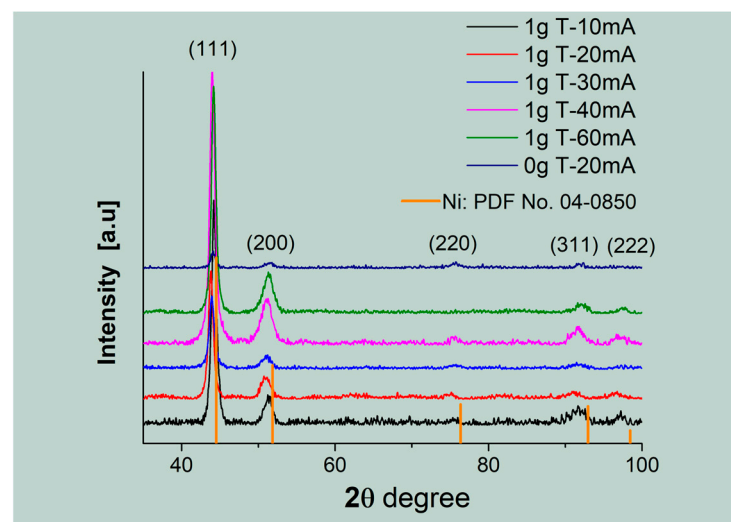

Figure 4. The XRD patterns of HEA coatings with 0 and 1 g/L saccharin deposited under various current densities (10, 20, 30, 40, and 60 mA/cm^2) for 60 min.

3.4. The Morphologies and Microstructures of FCCN-1g T Coatings Deposited at Various Current Densities

Figure 5 shows the typical scanning electron micrographs of FCCN-1g T coatings that were deposited at varying current densities. All the HEA coatings exhibit a relatively smooth surface morphology characterized by nodular structures of different sizes. The surfaces of the HEA coatings appear to be compact and free of cracks or pits, suggesting a more uniform distribution of the electric field during the crystal growth process with the addition of saccharin. Furthermore, as the current density increases, the surface roughness of HEA coatings becomes more pronounced, resulting in an uneven distribution of the nodular grains. For instance, in the case of the HEA coating deposited at 40 mA/cm^2, the

small nodular grains have a size of approximately 5 μm, while the larger nodular grains can reach up to 40 μm. This disparity in grain size seems to be a consequence of the increasing deposition rate of metal ions attributed to the higher current density.
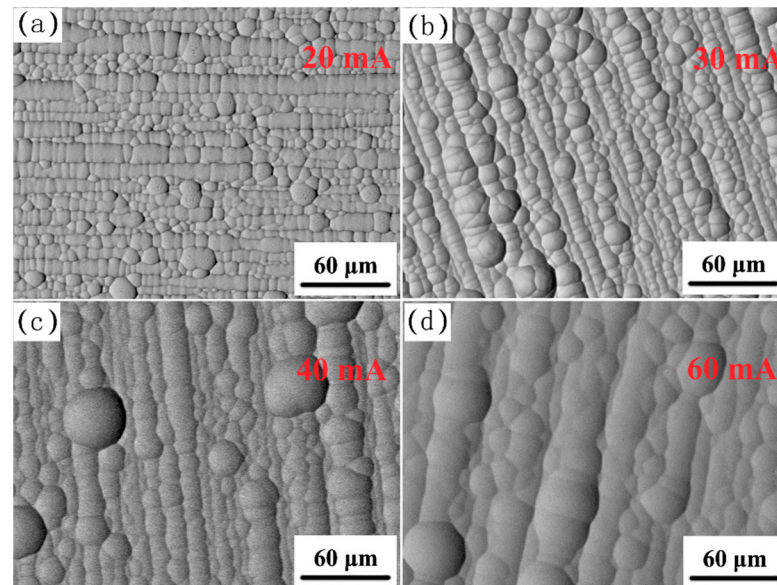

Figure 5. Secondary electron micrographs of HEA coatings deposited using 20 mA/cm^2 (**a**), 30 mA/cm^2 (**b**), 40 mA/cm^2 (**c**), and 60 mA/cm^2 (**d**) in a 1 g/L saccharin electrolyte for 60 min, respectively.

The surface EDS mappings in Figure 6 display the homogeneous distribution of Co, Fe, Ni, and Cu elements in the FCCN-1g T-20mA coatings, which suggests that electrodeposition can be considered as a practical technique for preparing HEA materials with a uniformly distributed structure. The elemental contents of FCCN coatings are presented in Table 2, demonstrating that the coatings comprise the four elements in approximately equimolar ratios.
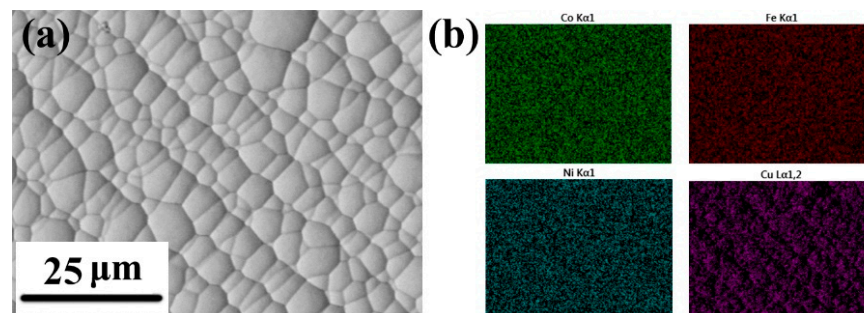

Figure 6. Scanning electron micrographs of a FCCN-1g T-20mA (1 g/L saccharin and deposition current density of 20 mA/cm^2) coating (**a**) and the corresponding elemental distribution maps of Co, Fe, Ni, and Cu, respectively (**b**).

Table 2. The elemental contents of FCCN coatings without and with 1 g/L saccharin addition.

Element (at. %)\Sample	0g T-20mA	0g T-40mA	1g T-10mA	1g T-20mA	1g T-30mA	1g T-40mA	1g T-60mA
Ni	42.61	38.15	31.32	28.31	36.81	32.52	54.71
Co	28.12	32.38	34.95	32.32	33.09	33.36	23.96
Fe	18.25	21.26	12.17	16.25	16.16	14.67	10.02
Cu	11.02	8.21	21.56	23.12	13.94	19.45	11.31

4. Discussion

4.1. Effect of Saccharin on the Cyclic Voltammograms

Saccharin is a commonly used green electroplating additive widely employed in nickel, chromium, and copper plating [50]. It has the effect of refining the grain sizes and reducing the internal stress of the deposits. From the cyclic voltammetry curve, compared with the solution without saccharin, the addition of saccharin leads to a noticeable cathodic peak in the reduction current during the negative voltage scan, which can be attributed to the co-deposition of multi-metal ions. Similar cyclic voltammograms have been reported for nickel deposition [55]. The occurrence of current loops forming upon reverse scanning towards the positive direction near a voltage of about −1.0 V indicates the nucleation and growth mechanism for metal-ion depositions [56]. As a result, the co-deposition of multi-metal ions in the electrolyte solution follows the classical nucleation–growth mechanism [49]. The reduction peaks associated with the mechanism of metal-ion deposition are of vital importance. The reduction peak positions in the cyclic voltammograms with different saccharin additions are located near a voltage of 0.6 V, and it should be noted that the cyclic voltammogram without saccharin exhibits the smallest reduction current, implying the accelerating effect of saccharin on the deposition of a multi-metal ion solution. It is noted that when saccharin is added beyond a certain amount (>2 g/L), the current becomes less. Although saccharin could weaken the anomalous co-deposition of the FeCoNi alloy, slightly increasing the deposition rate and efficiency, excessive saccharin concentrations may result in a weakening of cathodic polarization, ultimately reducing the reduction current [57,58]. Hence, a comprehensive investigation of electro-depositions has been conducted on the electrolyte containing 1 g/L saccharin, and the subsequent results will now be presented.

4.2. Effect of Saccharin on the Morphologies and Microstructures

During electrodeposition, saccharin in the solution can act as a leveling and brightening agent [50]. From a microscopic perspective, the cathode surface is not perfectly flat. The protruding region of the growing front on the cathode during electrodeposition has a higher electric field strength, resulting in a greater current density and preferential reduction of metal ions. Consequently, the Cu^{2+} ions with the lowest standard reduction potential were preferentially deposited, thereby forming the cauliflower-like structure, as shown in Figure 1a. Conversely, the HEA coatings deposited exhibit a considerably smoother and even appearance with saccharin addition. FCCN-0.5g T demonstrates a nodular surface morphology, with nodules having an average size of approximately 100–300 μm, which can be attributed to the adsorption of saccharin molecules on the active sites of the cathode. The adsorption of saccharin molecules on the cathode could reduce the growth rate by impeding the surface diffusion of ions [59], resulting in the uniform deposition and distribution of various alloying elements. With the addition of saccharin, the composition of the HEA becomes more uniform, with smaller differences in molar fractions among the four elements, compared to that of FCCN-0g T, as shown in Table 2. In addition, by increasing the saccharin content, the surface morphologies of the HEA coatings become flatter and more even.

The results of X-ray diffraction indicate that all the FCCN coatings exhibit a typical FCC structure without other phase constituents, because all of the diffraction peaks observed can be correlated to the powder diffraction peaks of nickel (PDF Card No. 04-0850, as shown in Figure 4). It is noteworthy that there is a slight angular deviation between the diffraction peaks of the FCCN deposits and those of standard nickel. This deviation is caused by the slight difference in the lattice constant of the high-entropy alloy solid solution and that of nickel. The grain sizes and RTCs (relative texture coefficients) of the HEA coatings are tabulated in Table 3. It can be observed that the addition of saccharin results in a decrease in the grain sizes of the HEA coatings, with the FCCN-1g T-20mA sample exhibiting the smallest grain size of 18.4 nm. This trend indicates the grain refinement effect of saccharin, which aligns with previous reports [50]. The FCCN-0g T samples electrodeposited at 20 and 40 mA/cm^2 exhibit a pronounced texture of a (1 0 0) orientation. However, with the

addition of saccharin, the texture of the HEA coatings gradually shifts towards the (2 0 0) orientation, and the addition of saccharin could function as an inhibitor of (1 0 0) growth for the HEA, providing more nucleation sites, and leading to grain refinement.

Table 3. The grain size and relative texture coefficients (RTC) of the coatings.

Sample ID	Grain Size (111) nm	Grain Size (200) nm	RTC_{111}	RTC_{200}	RTC_{220}	RTC_{311}
1g T-10mA	20.6	17.1	0.451	0.125	0.087	0.155
1g T-20mA	19.3	15.8	0.412	0.144	0.096	0.101
1g T-30mA	19.3	17.2	0.545	0.204	0.086	0.166
1g T-40mA	18.4	14.8	0.521	0.134	0.069	0.104
1g T-60mA	20.1	15.5	0.644	0.205	0.074	0.077
0g T-20mA	23.4	19.8	0.316	0.215	0.251	0.265
0g T-40mA	21.1	18.6	0.226	0.131	0.339	0.305

4.3. Effect of Current Density on the Morphologies, Compositions, and Microstructures of FCCN-1g T Coatings

The current density is one of the important parameters in the electrodeposition process [51]. To investigate the impact of the current density on the compositions and microstructures of HEA coatings, the FCCN-1g T was investigated as a model system to find out the effect of the current density on morphologies, compositions, and microstructures.

As the current density increases, the surface roughness of FCCN-1g T coatings becomes more pronounced, resulting in an uneven distribution of the nodular grains (Figure 5). For instance, in the case of the HEA coating deposited at 40 mA/cm^2, the small nodular grains have a size of approximately 5 μm, while the larger nodular grains can reach up to 40 μm. This disparity in grain size seems to be a consequence of increasing the deposition rate of metal ions attributed to a higher current density. Moreover, the intensity of RTC_{111} decreases while that of RTC_{200} increases as the current density increases. These changes suggest a preference for metal ions to selectively deposit on (2 0 0) crystal planes under a higher current density. A similar result has been observed in electrodeposited copper [60], where metal ions tend to preferentially deposit on (1 1 1) planes and grow along the <1 1 1> direction to minimize the total surface energy.

Although the standard reduction potentials of the four elements (Ni = 0.25 V, Fe = 0.44 V, Co = 0.28 V, and Cu = 0.34 V) varied considerably, with the Cu element in particular having the highest standard reduction potential, the EDS results indicated that the four elements could be successfully co-deposited to produce a uniform high-entropy alloy coating. At lower current densities (10–20 mA/cm^2), the molar fractions among the four elements are closer to each other. However, as the current density increases, the copper content decreases while the nickel content increases noticeably, which is similar to the previous report [61]. The alterations in the cobalt and iron contents exhibit less significant variations in response to changes in current densities, indicating that an equimolar fraction of HEAs could be derived by adjusting the current densities. Consequently, electrodeposition emerges as a practical technique for preparing HEA materials with uniformly distributed structures and controllable compositions.

4.4. Corrosion Properties of the FCCN-1g T Coatings

The results of the polarization tests for the FCCN coatings conducted in a 3.5 wt.% sodium chloride solution are presented in Figure 7. The critical parameters obtained through the Tafel tests, namely the open circuit potential (E_{corr}), corrosion current density (i_{corr}), and Tafel slopes (β_a and β_c), have been determined by the Tafel extrapolation method [52]. It is known that i_{corr} represents the corrosion rate and durability of coatings under similar corrosive environments, making it a useful parameter for comparing the anti-corrosion properties of different FCCN coatings. Compared to FCCN-0g T-20mA, which has the highest values of i_{corr} and a negative E_{corr} of −0.397 V, the E_{corr} value of

FCCN-1g T coatings noticeably decreases, and the E_{corr} value shifts towards a more positive direction with the introduction of saccharin. The i_{corr} value of the FCCN-1g T coating is approximately one order of magnitude lower than that of the FCCN-0g T deposit, indicating a remarkable improvement in protective properties. This trend confirms the comprehensive beneficial effect resulting from the formation of dense, homogeneous coatings with the incorporation of saccharin.
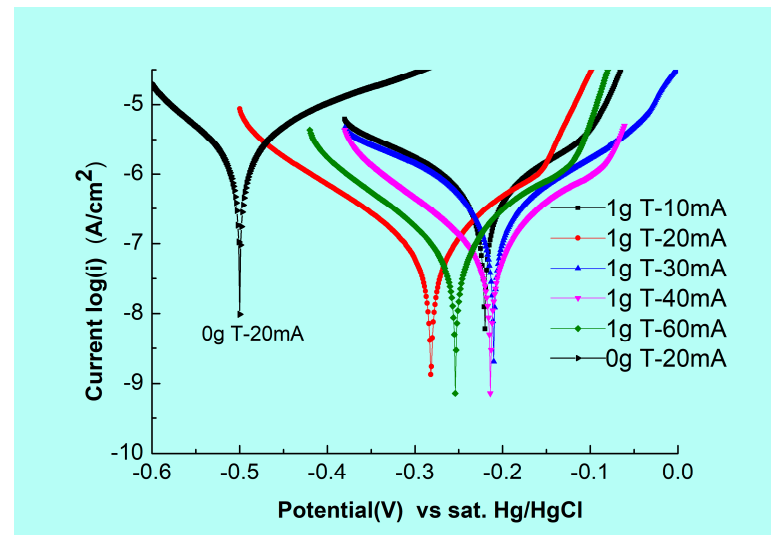

Figure 7. Polarization curves in semilogarithmic coordinates for the investigated alloy deposits in 3.5 wt.% NaCl (25 °C, 1 mV/s).

Figure 8 illustrates the Electrochemical Impedance Spectroscopy (EIS) results of FCCN-1g T coatings immersed in a 3.5 wt.% NaCl solution with a frequency range of 0.01 Hz to 100 kHz. The Nyquist plots exhibit depressed semicircles of varying sizes, suggesting that all FCCN-1g T coatings display a similar corrosion mechanism within this frequency range. Notably, the impedance-arc sizes of the FCCN-1g T-20mA and FCCN-1g T-60mA coatings are obviously larger than the others, indicating better anti-corrosion properties in the 3.5 wt.% NaCl solution compared to other samples. These EIS results align with the findings of previous Tafel polarization studies. To gain a better understanding of the corrosion mechanism at the open circuit potential, the EIS data were fitted to an electrical equivalent circuit (EEC), as shown in Figure 8c, which is characterized by two time constants that correspond to two close capacitive loops. Because of the dispersing effect of capacitive loops, the electrode is not a pure capacitor, and a constant-phase element (CPE) is used to replace the ideal capacitor on the surface, which can be defined as follows:

$$Z_{CPE} = \frac{1}{Q(j\omega)^n} \tag{3}$$

where j denotes the imaginary unit, Q represents the CPE constant, n is an empirical constant with values from 0 to 1, and ω represents the frequency. Therefore, the EEC includes the following: non-ideal coating capacitance (CPE1), double-layer capacitance (CPE2), charge transfer resistance (R_{ct}), coating resistance (R_{coat}), and solution resistance (R_s). The analysis of the EEC parameters was carried out, using the ZVIEW software [62], and the values of these parameters in the EEC are presented in Table 4, suggesting that the FCCN-1g T coatings with saccharin addition of 1 g/L demonstrate better corrosion resistance compared to the one without saccharin addition, which is aligned with the impedance loops shown in Figure 8a,b. The aggressive ions in the solution, e.g., Cl⁻, would attack the passivation film, resulting in a decrease in impedance value [63]. It is known that a higher R_{ct} and lower electron transfer value are correlated to higher corrosion resistance [41]. Specifically, the FCCN-1g T-20mA coating demonstrates the lowest i_{corr}

value of 0.34 µA/cm^2 and the highest charge transfer resistance of 48,170 Ωcm^2, indicating that the passive film formed on the HEA surface was denser and provided higher protective performance. However, a further increase in the deposition current density leads to a decline in corrosion resistance with the formation of increasingly uneven microstructures. Interestingly, when the deposition current density is increased to 60 mA/cm^2, the i$_{corr}$ decreases to 0.46 µA/cm^2, and R$_{ct}$ increases up to 39,170 Ωcm^2, suggesting an improvement in corrosion-resistant properties for FCCN-1g T-60mA, compared to those of FCCN-1g T-30mA and FCCN-1g T-40mA. This phenomenon could be attributed to changes in the composition of the FCCN-1g T at higher current densities. As the current density increases, the nickel content rises to 50%, while the iron content decreases to its minimum among all samples. Since the iron element exhibits a lower corrosion potential, compared to other elements, the FCCN-1g T sample deposited at 60 mA/cm^2 demonstrates a partial recovery in its anti-corrosion property.
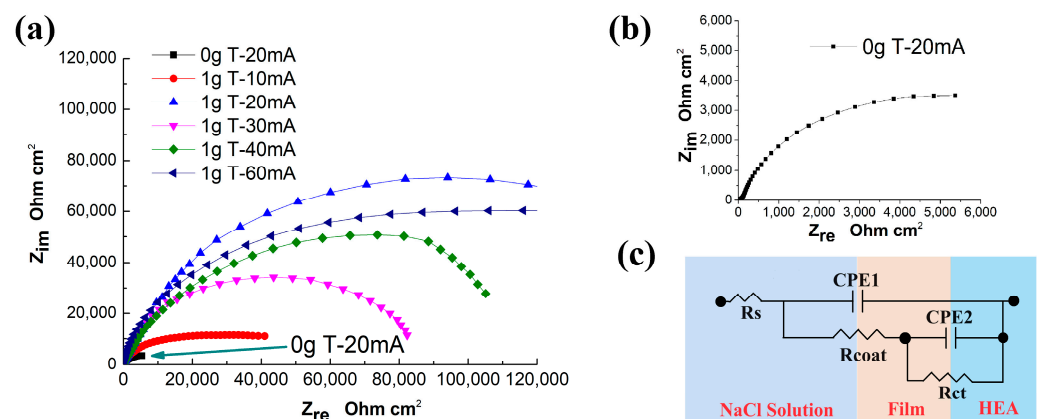

Figure 8. Nyquist plots for the investigated alloy deposits in 3.5 wt.% NaCl at open circuit potential (**a**) (solid lines are the fit to the measured points using the equivalent circuit shown in (**c**)), enlarged plot for the FCCN-0g T-20mA (**b**), and the equivalent circuit (**c**).

Table 4. Values of corrosion parameters determined from polarization curves and fitting of impedance spectra using the equivalent circuit proposed in Figure 8c.

Sample	E$_{corr}$ (V)	i$_{corr}$ (µA/cm^2)	β$_a$ (V/dec)	β$_c$ (V/dec)	CPE1 (µFcm^{-2})	CPE2 (µFcm^{-2})	R$_{ct}$ (Ωcm^2)
0g T-20mA	−0.397	9.52	0.1612	0.1385	50.2	15.2	3245
1g T-10mA	−0.201	2.23	0.1357	0.1493	10.3	7.8	12,600
1g T-20mA	−0.245	0.41	0.1198	0.1217	5.1	3.4	48,170
1g T-30mA	−0.117	1.31	0.1305	0.1610	8.6	6.8	29,065
1g T-40mA	−0.223	0.88	0.0992	0.1151	17.2	8.6	35,632
1g T-60mA	−0.229	0.46	0.1350	0.1079	18.5	14.1	39,170

Corrosion resistance is one of the crucial performance indicators for electrodeposited HEA coatings used for a protective purpose. Previous studies have usually employed the addition of inert reinforcing agents, such as a graphene oxide (GO) [41] and carbon nanotubes [64], to enhance the stability of the HEA matrix and improve its corrosion resistance. These inert reinforcement phases aid in the formation of stable oxide layers on the surface of the HEA coatings, thereby hindering the diffusion of ions and significantly enhancing their corrosion resistance, often by an order of magnitude, compared to the HEA coatings without such reinforcement. In addition, Michel et al. [42] propose an alternative approach for the development of high-quality MoW-containing HEAs through electrodeposition from an aqueous solution, but primarily with an amorphous structure. However, in the present study, we demonstrate remarkable improvements in the structure and corrosion resistance of HEA coatings by simply adjusting the concentration of the

economical saccharin and current density during the electrodeposition process. This promising pathway highlights the potential of electrodeposition from aqueous solutions for high-quality HEA systems. Future research can focus on further optimizing process parameters and incorporating reinforcing agents into the electrolyte system to achieve even better overall performance.

5. Conclusions

In this study, we explored the influence of additives and current densities on the compositions, surface morphologies, microstructures, and corrosion behavior of the electrodeposited NiFeCoCu alloy coatings. The primary findings are summarized as follows:

1. The study demonstrates the crucial role of saccharin in achieving a smooth and lustrous surface for NiFeCoCu coatings, while also alleviating the internal stress and enhancing their corrosion resistances.
2. Notably, electrodeposition performed at a current density ranging from 20 to 40 mA/cm^2 yielded a homogeneous and compact coating with favorable anticorrosion properties.
3. The FCCN-1g T-20mA coatings deposited using a current density of 20 mA/cm^2 display a near-equimolar composition and the best anti-corrosion property with an i_{corr} of 0.34 μA/cm^2 in a simulated seawater solution.
4. The present research presents a cost-effective and viable industrial approach for fabricating HEA coatings, holding remarkable potential for advancing innovation in the field of electrodeposited HEA coatings.

Author Contributions: Conceptualization, Y.W. and N.Z.; methodology, Y.W. and S.Y.; validation, B.M. and P.K.L.; investigation, Y.W. and N.Z.; resources, W.L.; writing—original draft preparation, N.Z.; writing—review and editing, W.L. and P.K.L.; supervision, N.Z.; project administration, W.L. and N.Z.; funding acquisition, W.L. and P.K.L. All authors have read and agreed to the published version of the manuscript.

Data Availability Statement: The raw data supporting the conclusions of this article will be made available by the authors on request.

Conflicts of Interest: The authors declare no conflicts of interest.

References

1. Cantor, B.; Chang, I.T.H.; Knight, P.; Vincent, A.J.B. Microstructural Development in Equiatomic Multicomponent Alloys. *Mater. Sci. Eng. A* **2004**, *375–377*, 213–218. [CrossRef]
2. Yeh, J.-W.; Chen, S.-K.; Lin, S.-J.; Gan, J.-Y.; Chin, T.-S.; Shun, T.-T.; Tsau, C.-H.; Chang, S.-Y. Nanostructured High-Entropy Alloys with Multiple Principal Elements: Novel Alloy Design Concepts and Outcomes. *Adv. Eng. Mater.* **2004**, *6*, 299–303. [CrossRef]
3. Zhang, Y.; Zuo, T.T.; Tang, Z.; Gao, M.C.; Dahmen, K.A.; Liaw, P.K.; Lu, Z.P. Microstructures and Properties of High-Entropy Alloys. *Prog. Mater. Sci.* **2014**, *61*, 1–93. [CrossRef]
4. Das, S.; Nishad, S.; Robi, P. A New High-Entropy Alloy of Al-Fe-Co-Ni-Cu Possessing Single Face-Centered Cubic Crystal Structure and Excellent Mechanical Properties at Room Temperature. *Phys. Status Solidi Appl. Mater. Sci.* **2021**, *218*, 2000825. [CrossRef]
5. Liu, H.; Gu, C.; Zhai, K.; Wang, C. Strengthening and Toughening the FeNiCrMn Medium Entropy Alloy by Novel Ultrafine Precipitate Networks. *Vacuum* **2021**, *184*, 109995. [CrossRef]
6. Gludovatz, B.; Hohenwarter, A.; Catoor, D.; Chang, E.H.; George, E.P.; Ritchie, R.O. A Fracture-Resistant High-Entropy Alloy for Cryogenic Applications. *Science* **2014**, *345*, 1153–1158. [CrossRef]
7. Pan, Q.; Zhang, L.; Feng, R.; Lu, Q.; An, K.; Chuang, A.C.; Poplawsky, J.D.; Liaw, P.K.; Lu, L. Gradient Cell–Structured High-Entropy Alloy with Exceptional Strength and Ductility. *Science* **2021**, *374*, 984–989. [CrossRef]

8. Shi, P.; Li, R.; Li, Y.; Wen, Y.; Zhong, Y.; Ren, W.; Shen, Z.; Zheng, T.; Peng, J.; Liang, X.; et al. Hierarchical Crack Buffering Triples Ductility in Eutectic Herringbone High-Entropy Alloys. *Science* **2021**, *373*, 912–918. [CrossRef]

9. Dada, M.; Popoola, P.; Mathe, N.; Pityana, S.; Adeosun, S. In-Situ Reactive Synthesis and Characterization of a High Entropy Alloy Coating by Laser Metal Deposition. *Int. J. Lightweight Mater. Manuf.* **2022**, *5*, 11–19. [CrossRef]

10. Serban, B.-A.; Olaru, M.-T.; Badea, I.-C.; Mitrica, D.; Burada, M.; Anasiei, I.; Ghita, M.; Tudor, A.-I.; Matei, C.-A.; Popescu, A.M.J.; et al. Non-Aqueous Electrodeposition and Characterization of AlCrCuFeNi High Entropy Alloy Thin Films. *Materials* **2022**, *15*, 6007. [CrossRef]

11. Shi, Y.; Yang, B.; Liaw, P.K. Corrosion-Resistant High-Entropy Alloys: A Review. *Metals* **2017**, *7*, 43. [CrossRef]

12. Shi, Y.; Yang, B.; Xie, X.; Brechtl, J.; Dahmen, K.A.; Liaw, P.K. Corrosion of AlxCoCrFeNi High-Entropy Alloys: Al-Content and Potential Scan-Rate Dependent Pitting Behavior. *Corros. Sci.* **2017**, *119*, 33–45. [CrossRef]

13. Bhattacharyya, J.J.; Inman, S.B.; Wischhusen, M.A.; Qi, J.; Poon, J.; Scully, J.R.; Agnew, S.R. Lightweight, Low Cost Compositionally Complex Multiphase Alloys with Optimized Strength, Ductility and Corrosion Resistance: Discovery, Design and Mechanistic Understandings. *Mater. Des.* **2023**, *228*, 111831. [CrossRef]

14. Li, T.; Swanson, O.J.; Frankel, G.S.; Gerard, A.Y.; Lu, P.; Saal, J.E.; Scully, J.R. Localized Corrosion Behavior of a Single-Phase Non-Equimolar High Entropy Alloy. *Electrochim. Acta* **2019**, *306*, 71–84. [CrossRef]

15. Zhou, E.; Qiao, D.; Yang, Y.; Xu, D.; Lu, Y.; Wang, J.; Smith, J.A.; Li, H.; Zhao, H.; Liaw, P.K.; et al. A Novel Cu-Bearing High-Entropy Alloy with Significant Antibacterial Behavior against Corrosive Marine Biofilms. *J. Mater. Sci. Technol.* **2020**, *46*, 201–210. [CrossRef]

16. Pavithra, C.L.P.; Janardhana, R.K.S.K.; Reddy, K.M.; Murapaka, C.; Joardar, J.; Sarada, B.; Tamboli, R.R.; Hu, Y.; Zhang, Y.; Wang, X.; et al. An Advancement in the Synthesis of Unique Soft Magnetic CoCuFeNiZn High Entropy Alloy Thin Films. *Sci. Rep.* **2021**, *11*, 8836. [CrossRef] [PubMed]

17. Glasscott, M.W.; Pendergast, A.D.; Goines, S.; Bishop, A.R.; Hoang, A.T.; Renault, C.; Dick, J.E. Electrosynthesis of High-Entropy Metallic Glass Nanoparticles for Designer, Multi-Functional Electrocatalysis. *Nat. Commun.* **2019**, *10*, 2650. [CrossRef] [PubMed]

18. Jiang, S.; Duan, C.; Li, X.; Wang, D.; Wang, Z.; Sun, H.; Zheng, R.; Liu, Y. Alloying Strategy for Constructing Multi-Component Nano-Catalysts towards Efficient and Durable Oxygen Evolution in Alkaline Electrolyte. *Electrochim. Acta* **2021**, *391*, 138933. [CrossRef]

19. Liu, L.; Yu, X.; Zhang, W.; Lv, Q.; Hou, L.; Fautrelle, Y.; Ren, Z.; Cao, G.; Lu, X.; Li, X. Strong Magnetic-Field-Engineered Porous Template for Fabricating Hierarchical Porous Ni-Co-Zn-P Nanoplate Arrays as Battery-Type Electrodes of Advanced All-Solid-State Supercapacitors. *ACS Appl. Mater. Interfaces* **2022**, *14*, 2782–2793. [CrossRef] [PubMed]

20. He, L.; Wang, N.; Sun, B.; Zhong, L.; Yao, M.; Hu, W.; Komarneni, S. High-Entropy FeCoNiMn (Oxy)Hydroxide as High-Performance Electrocatalyst for OER and Boosting Clean Carrier Production under Quasi-Industrial Condition. *J. Clean. Prod.* **2022**, *356*, 131680. [CrossRef]

21. Chen, Y.Y.; Duval, T.; Hung, U.D.; Yeh, J.W.; Shih, H.C. Microstructure and Electrochemical Properties of High Entropy Alloys—A Comparison with Type-304 Stainless Steel. *Corros. Sci.* **2005**, *47*, 2257–2279. [CrossRef]

22. Izadi, M.; Soltanieh, M.; Alamolhoda, S.; Aghamiri, S.M.S.; Mehdizade, M. Microstructural Characterization and Corrosion Behavior of AlxCoCrFeNi High Entropy Alloys. *Mater. Chem. Phys.* **2021**, *273*, 124937. [CrossRef]

23. Liang, H.; Miao, J.; Gao, B.; Deng, D.; Wang, T.; Lu, Y.; Cao, Z.; Jiang, H.; Li, T.; Kang, H. Microstructure and Tribological Properties of $AlCrFe_2Ni_2W_{0.2}Mo_{0.75}$ High-Entropy Alloy Coating Prepared by Laser Cladding in Seawater, NaCl Solution and Deionized Water. *Surf. Coat. Technol.* **2020**, *400*, 126214. [CrossRef]

24. Zhang, P.; Xu, Z.; Yao, Z.; Liu, Y.; Lin, S.; He, M.; Lu, S.; Wu, X. A High-Corrosion-Resistant High-Entropy Alloys (HEAs) Coatings with Single BCC Solid Solution Structure by Laser Remelting. *Mater. Lett.* **2022**, *324*, 132728. [CrossRef]

25. Ma, P.; Fang, Y.; Wei, S.; Zhang, Z.; Yang, H.; Wan, S.; Prashanth, K.G.; Jia, Y. Microstructure and Mechanical Properties of AlCoCrFeMnNi HEAs Fabricated by Selective Laser Melting. *J. Mater. Res. Technol.* **2023**, *25*, 7090–7100. [CrossRef]

26. Braeckman, B.R.; Boydens, F.; Hidalgo, H.; Dutheil, P.; Jullien, M.; Thomann, A.-L.; Depla, D. High Entropy Alloy Thin Films Deposited by Magnetron Sputtering of Powder Targets. *Thin Solid Films* **2015**, *580*, 71–76. [CrossRef]

27. Wang, W.; Qi, W.; Zhang, X.; Yang, X.; Xie, L.; Li, D.; Xiang, Y. Superior Corrosion Resistance-Dependent Laser Energy Density in $(CoCrFeNi)_{95}Nb_5$ High Entropy Alloy Coating Fabricated by Laser Cladding. *Int. J. Miner. Metall. Mater.* **2021**, *28*, 888–897. [CrossRef]

28. Xiao, J.-K.; Tan, H.; Wu, Y.-Q.; Chen, J.; Zhang, C. Microstructure and Wear Behavior of FeCoNiCrMn High Entropy Alloy Coating Deposited by Plasma Spraying. *Surf. Coat. Technol.* **2020**, *385*, 125430. [CrossRef]

29. Li, H.; Li, J.; Yan, C.; Zhang, X.; Xiong, D. Microstructure and Tribological Properties of Plasma-Sprayed $Al_{0.2}Co_{1.5}CrFeNi_{1.5}Ti$-Ag Composite Coating from 25 to 750 °C. *J. Mater. Eng. Perform.* **2020**, *29*, 1640–1649. [CrossRef]

30. Huang, J.; Du, K.; Wang, P.; Yin, H.; Wang, D. Electrochemical Preparation and Homogenization of Face-Centered FeCoNiCu Medium Entropy Alloy Electrodes Enabling Oxygen Evolution Reactions. *Electrochim. Acta* **2021**, *378*, 138142. [CrossRef]

31. Guo, X.; Liu, P.; Xia, Y.; Dong, Z.; Liu, H.; Chen, Y. Two-Step Hydrogen Reduction of Oxides for Making FeCoNiCu High Entropy Alloy: Part I—Process and Mechanical Properties. *Mater. Charact.* **2022**, *193*, 112271. [CrossRef]

32. Yao, C.-Z.; Zhang, P.; Liu, M.; Li, G.-R.; Ye, J.-Q.; Liu, P.; Tong, Y.-X. Electrochemical Preparation and Magnetic Study of Bi-Fe-Co-Ni-Mn High Entropy Alloy. *Electrochim. Acta* **2008**, *53*, 8359–8365. [CrossRef]

33. Soare, V.; Burada, M.; Constantin, I.; Mitrica, D.; Badilita, V.; Caragea, A.; Tarcolea, M. Electrochemical Deposition and Microstructural Characterization of AlCrFeMnNi and AlCrCuFeMnNi High Entropy Alloy Thin Films. *Appl. Surf. Sci.* **2015**, *358*, 533–539. [CrossRef]

34. Yoosefan, F.; Ashrafi, A.; Vaghefi, S.M.M.; Constantin, I. Synthesis of CoCrFeMnNi High Entropy Alloy Thin Films by Pulse Electrodeposition: Part 1: Effect of Pulse Electrodeposition Parameters. *Met. Mater. Int.* **2020**, *26*, 1262–1269. [CrossRef]

35. Akbarpour, M.R.; Gharibi Asl, F.; Rashedi, H. Anti-Corrosion and Microstructural Properties of Nanostructured Ni-Co Coating Prepared by Pulse-Reverse Electrochemical Deposition Method. *J. Mater. Eng. Perform.* **2023**, *33*, 94–101. [CrossRef]

36. Aliyu, A.; Srivastava, C. Corrosion Behavior and Protective Film Constitution of AlNiCoFeCu and AlCrNiCoFeCu High Entropy Alloy Coatings. *Surf. Interfaces* **2021**, *27*, 101481. [CrossRef]

37. Yoosefan, F.; Ashrafi, A.; Monir Vaghefi, S.M. Microstructure and Corrosion Properties of Electrodeposited CoCrFeMnNi High Entropy Alloy Coatings. *Front. Mater.* **2022**, *9*, 891011. [CrossRef]

38. Yoosefan, F.; Ashrafi, A.; Monirvaghefi, S.M.; Constantin, I. Effect of Frequency Changes in Pulsed Deposition Process on the Composition and Morphology of CoCrFeMnNi High Entropy Alloy Coatings. *Metall. Eng.* **2020**, *23*, 245–254.

39. Omar, I.M.A.; Aziz, M.; Emran, K.M. Impact of Ionic Liquid [FPIM]Br on the Electrodeposition of Ni and Co from an Aqueous Sulfate Bath. *J. Mater. Res. Technol.* **2021**, *12*, 170–185. [CrossRef]

40. Pavithra, C.L.P.; Janardhana, R.K.S.K.; Reddy, K.M.; Murapaka, C.; Klement, U.; Dey, S.R. Graphene Oxide Reinforced Magnetic FeCoNiCuZn High Entropy Alloy through Electrodeposition. *J. Electrochem. Soc.* **2022**, *169*, 022501. [CrossRef]

41. Aliyu, A.; Srivastava, C. Phase Constitution, Surface Chemistry and Corrosion Behavior of Electrodeposited MnFeCoNiCu High Entropy Alloy-Graphene Oxide Composite Coatings. *Surf. Coat. Technol.* **2022**, *429*, 127943. [CrossRef]

42. Haché, M.J.R.; Tam, J.; Erb, U.; Zou, Y. Electrodeposited NiFeCo-(Mo,W) High-Entropy Alloys with Nanocrystalline and Amorphous Structures. *J. Alloys Compd.* **2023**, *952*, 170026. [CrossRef]

43. Aliyu, A.; Srivastava, C. Microstructure and Electrochemical Properties of FeNiCoCu Medium Entropy Alloy-Graphene Oxide Composite Coatings. *J. Alloys Compd.* **2021**, *864*, 158851. [CrossRef]

44. Hassan, M.A.; Ghayad, I.M.; Mohamed, A.S.A.; El-Nikhaily, A.E.; Elkady, O.A. Improvement Ductility and Corrosion Resistance of CoCrFeNi and AlCoCrFeNi HEAs by Electroless Copper Technique. *J. Mater. Res. Technol.* **2021**, *13*, 463–485. [CrossRef]

45. Zhao, Y.; Ma, H.; Zhang, L.; Zhang, D.; Kou, S.; Wang, B.; Li, W.; Liaw, P. Mn Content Optimum on Microstructures and Mechanical Behavior of Fe-Based Medium Entropy Alloys. *Mater. Des.* **2022**, *223*, 111241. [CrossRef]

46. Wu, C.; Zhou, C.; Liu, Y.; Peng, H.; Wang, J.; Su, X. Effects of Vacuum Annealing on the Phase Constituents and Mechanical Properties of the $Al_X CrFeMn_{2-X}Ni$ Multiprincipal Component Alloys. *Vacuum* **2022**, *199*, 110934. [CrossRef]

47. Yang, J.; Jiang, L.; Liu, Z.; Tang, Z.; Wu, A. Multifunctional Interstitial-Carbon-Doped FeCoNiCu High Entropy Alloys with Excellent Electromagnetic-Wave Absorption Performance. *J. Mater. Sci. Technol.* **2022**, *113*, 61–70. [CrossRef]

48. Tandon, P.; Mishra, A.C. The Effect of Magnetic Field Orientation on the Magnetoimpedance of Electroplated NiFeCo/Cu Wire. *J. Mater. Sci. Mater. Electron.* **2022**, *33*, 18311–18326. [CrossRef]

49. Marikkannu, K.R.; Kalaignan, G.P.; Vasudevan, T. The Role of Additives in the Electrodeposition of Nickel–Cobalt Alloy from Acetate Electrolyte. *J. Alloys Compd.* **2007**, *438*, 332–336. [CrossRef]

50. Bakhit, B.; Akbari, A. A Comparative Study of the Effects of Saccharin and β-SiC Nano-Particles on the Properties of Ni and Ni–Co Alloy Coatings. *Surf. Coat. Technol.* **2014**, *253*, 76–82. [CrossRef]

51. Brenner, A. *Electrodeposition of Alloys: Principles and Practice*; Academic Press: New York, NY, USA; London, UK, 1963.

52. McCafferty, E. Validation of Corrosion Rates Measured by the Tafel Extrapolation Method. *Corros. Sci.* **2005**, *47*, 3202–3215. [CrossRef]

53. Klug, H.P.; Alexander, A.L. *X-ray Diffraction Procedures: For Polycrystalline and Amorphous Materials*, 2nd ed.; Wiley: Hoboken, NJ, USA, 1974.

54. Nik Masdek, N.R.; Alfantazi, A.M. An EQCM Study on the Influence of Saccharin on the Corrosion Properties of Nanostructured Cobalt and Cobalt-Iron Alloy Coatings. *J. Solid State Electrochem.* **2014**, *18*, 1701–1716. [CrossRef]

55. King, M.K.; Mahapatra, M.K. Microstructure of Electrodeposited Nickel: Role of Additives. *J. Mater. Eng. Perform.* **2020**, *29*, 7555–7566. [CrossRef]

56. Moharana, M.; Mallik, A. Nickel Electrocrystallization in Different Electrolytes: An in-Process and Post Synthesis Analysis. *Electrochim. Acta* **2013**, *98*, 1–10. [CrossRef]

57. Yu, J.; Wang, M.; Li, Q.; Yang, J.; Liu, L. Effects of Saccharin on Microstructure and Property of Electro-Deposited Ni-Fe Alloys. *Trans. Nonferrous Met. Soc. China* **2009**, *19*, 805–809. [CrossRef]

58. Fukuda, K.; Kashiwa, Y.; Oue, S.; Takasu, T.; Nakano, H. Effect of Additives on the Deposition Behavior and Micro Structure of Invar Fe–Ni Alloys with Low Thermal Expansion Electrodeposited from Watt's Solution. *ISIJ Int.* **2021**, *61*, 919–928. [CrossRef]

59. Hassani, S.; Raeissi, K.; Golozar, M.A. Effects of Saccharin on the Electrodeposition of Ni–Co Nanocrystalline Coatings. *J. Appl. Electrochem.* **2008**, *38*, 689–694. [CrossRef]

60. Deng, Y.; Ling, H.; Feng, X.; Hang, T.; Li, M. Electrodeposition and Characterization of Copper Nanocone Structures. *CrystEngComm* **2014**, *17*, 868–876. [CrossRef]

61. Bradley, P.E.; Janossy, B.; Landolt, D. Pulse Plating of Cobalt–Iron–Copper Alloys. *J. Appl. Electrochem.* **2001**, *31*, 137–144. [CrossRef]

62. Liu, Q.; Zhou, B.; Zhang, J.; Zhang, W.; Zhao, M.; Li, N.; Xiong, M.; Chen, J.; Yu, Y.; Song, S. Influence of Ru-Ni-Nb Combined Cathode Modification on Corrosion Behavior and Passive Film Characteristics of Ti-6Al-4V Alloy Used for Oil Country Tubular Goods. *Corros. Sci.* **2022**, *207*, 110569. [CrossRef]
63. Ye, Y.; Zhang, D.; Liu, Z.; Liu, W.; Zhao, H.; Wang, L.; Li, X. Anti-Corrosion Properties of Oligoaniline Modified Silica Hybrid Coatings for Low-Carbon Steel. *Synth. Met.* **2018**, *235*, 61–70. [CrossRef]
64. Singh, S.; Srivastava, C. On the Evolution of Protective Oxide Chemistry and Corrosion Resistance of Electrodeposited FeCrMnNiCo-Carbon Nanotube Composite Coatings. *Philos. Mag.* **2023**, *103*, 507–530. [CrossRef]